Use of SWIR Imaging to Monitor Layer-to-Layer Part Quality during SLM of 304L Stainless Steel

Cody S. Lough, Xin Wang, Christopher C. Smith, Olaseni Adeniji,
Robert G. Landers, Douglas A. Bristow, Edward C. Kinzel

Abstract

This paper evaluates using in-situ SWIR imaging to monitor part quality and identify potential defect locations introduced during Selective Laser Melting (SLM) of 304L stainless steel. The microstructure (porosity, grain size, and phase field) and engineering properties (density, modulus, and yield strength) depend on the thermal history during SLM manufacturing. Tensile test specimens have been built with a Renishaw AM250 using varied processing conditions to generate different thermal histories. SWIR imaging data is processed layer-to-layer to extract features in the thermal history for each process condition. The features in the thermal history are correlated with resulting part engineering properties, microstructure, and defects. The use of SWIR imaging is then discussed as a potential for processes monitoring to ensure part quality and develop layer-to-layer control in SLM. This work was funded by Honeywell Federal Manufacturing & Technologies under Contract No. DE-NA0002839 with the U.S. Department of Energy.

1. Introduction

Selective Laser Melting (SLM) is a powder bed additive manufacturing (AM) process in which 3-Dimensional metal parts are produced layer by layer. During SLM, a laser scans and fuses the metal powder bed along paths defined by the part geometry with preset process parameters. The SLM process parameters determine the thermal histories parts experience during manufacturing. The thermal history ultimately controls the microstructure and mechanical properties. Monitoring the thermal history using layer-to-layer infrared imaging gives insight into the SLM process with the potential to ensure part quality.

Researchers have used infrared and visible imaging to understand the thermal history parts experience during manufacturing and gain information about the melt pool. Long-wave infrared (LWIR) cameras are used to monitor slower dynamics at lower temperatures during SLM. Krauss et al. used a detector sensitive in the LWIR (8-14 µm) to characterize the heat affected zone during SLM of Inconel 718 for variations in laser scan strategies. The detector was used to find and compare off nominal features in the thermal history of the heat affected zone near borders of parts and overhangs. Grasso et al. monitored the SLM process of zinc powder with an infrared camera sensitive from 8-9 µm. The camera was incorporated to monitor the stability of the process and was able to identify the beginning of SLM process failure during layer-to-layer monitoring.

Visible and short-wave infrared (SWIR) cameras are used to monitor faster dynamics in the SLM process and measure melt pool features. Yadroitsev et al. developed an SLM monitoring system with a CCD camera to measure the surface temperature and melt pool size during processing Ti6Al4V. Findings included the maximum temperature of the melt pool was experienced large increases for processing with higher laser powers, but only small increases for higher exposure times. The width and the depth of the melt pool were determined to scale with

changes temperature as a result of processing with varied laser parameters. Heigel and Lane analyzed the effects of powder on the melt pool size and cooling rates experienced during SLM through process monitoring with a SWIR camera. The SWIR imaging data showed an increase in melt pool length and lower cooling rates for processing powder. Cheng et al. used a SWIR camera to monitor melt pool size as a function of build height during SLM of Monel K500. Build height was determined to not significantly affect the melt pool size.

Most researchers use infrared imaging to understand the temperature and size of the melt pool evolve during manufacturing while some researchers monitor the thermal history to identify defects in the SLM process. In this paper, SWIR imaging is used in layer-to-layer process monitoring during SLM of 304L stainless steel. Thermal features are extracted from the SWIR imaging data to identify defects in 3-Dimensional reconstructions of the SLM parts. These features are related to the melt pool size and SLM process parameters used during manufacturing. The thermal features are then correlated to part engineering properties to understand how data from the thermal history relate to mechanical performance. This is done to ultimately understand if meaningful information can be obtained from the SWIR data to ensure part quality and use in controls oriented decision making.

2. Experimental Setup

A Renishaw AM250 SLM system was used to manufacture cylindrical tensile test specimens (ASTM E8/E8M) out of 304L stainless steel (layer thickness of 50 µm). The Renishaw AM250 uses a 200 W maximum fiber laser ($\lambda = 1070$ nm) that scans with a point-to-point exposure strategy. In the point-to-point exposure strategy, the laser scanning parameters include power, P, exposure time, t_e, point distance, d_p, and hatch spacing, hs. The laser steps along the scan path by the point distance and then emits for the exposure time. To simplify process parameters into a single term, linear energy density, E_ρ, can be calculated using Eq. 1.

$$E_\rho = \frac{P \cdot t_e}{d_p} \tag{1}$$

In this work, the tensile specimens were manufactured with constant point distance (60 µm) and hatch spacing (85 µm) while the laser power (100, 125, 150, 175, 200 W) and exposure time (50, 75, 100, 125 µs) were varied. SWIR imaging data was collected in-situ during the SLM manufacturing process for all combinations of laser power and exposure time. Figure 1 (a) is a schematic of the AM250 build chamber with the SWIR camera mounted at a fixed location. The SWIR imaging data was collected through a window installed on the top of the AM250 build chamber. A notch filter was selected to protect the camera from scattered laser radiation and a bandpass filter was utilized to minimize saturation in the thermal data.
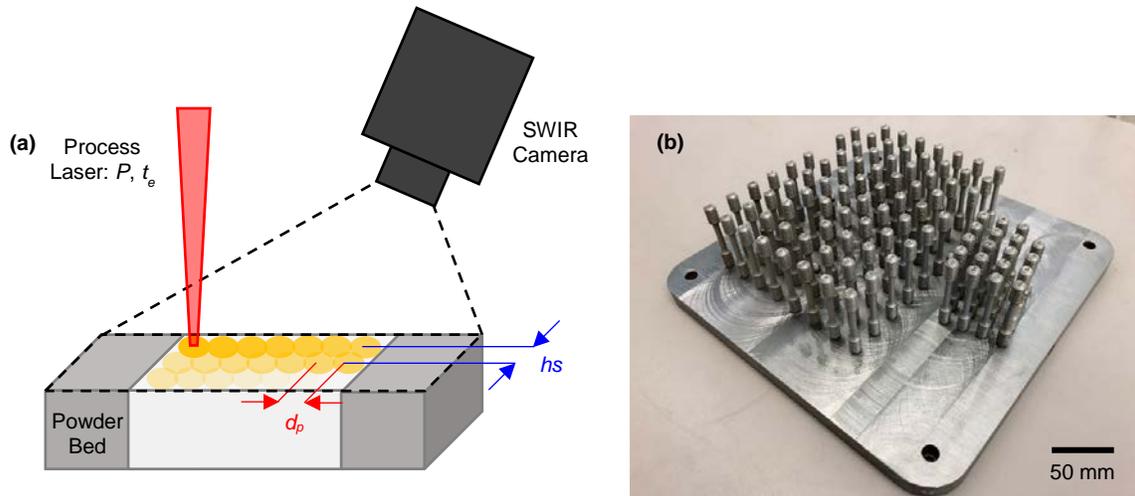
FIG 1: (a) Schematic of AM250 building process with SWIR camera observing powder bed and (b) completed build of tensile test specimens.

Three additional tensile test tensile test specimens were manufactured for layer-to-layer observations using a laser power of 200 W and exposure time of 75 μs. Two of the specimens were manufactured with introduced defects. This was done to demonstrate the ability to detect the defects with in-situ measurements taken with the SWIR camera. A nominal specimen was built for comparison to the defect specimens.

3. Thermal Camera Data Processing

3.1. Thermal Feature Extraction

Preforming layer-to-layer observations with the SWIR camera results in time-series data of the laser processing each slice of the tensile test specimen geometry. Figure 2 contains images of the apparent melt pool from selected frames in the time series data for two process parameter combinations. Features can be extracted from this time series thermal data to assign a value to each pixel for compression to a single representative frame for each layer. The pixels in the representative frames have a known size in object space and a third dimension corresponding to the layer thickness can be assigned to create a voxel. A filter for the voxel based data is determined by the thermal feature extracted from the time-series recordings of the layers. In this paper, the time above melt temperature, maximum spatial gradient, and maximum cooling rate are extracted from the time series thermal data for comparison.
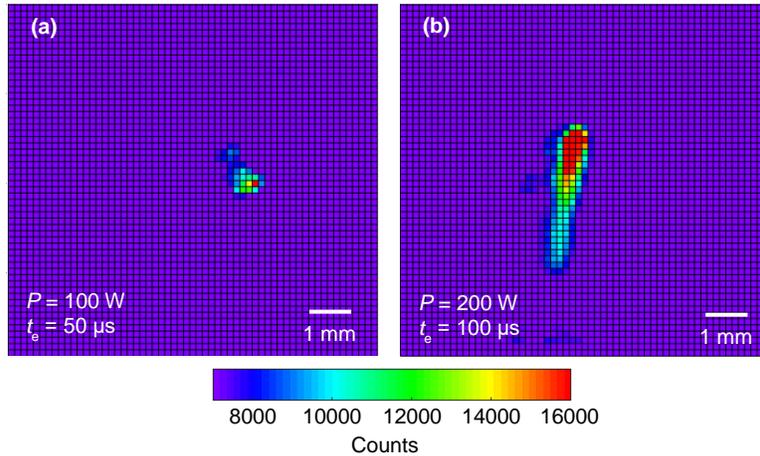
FIG 2: Images of melt pools from SWIR camera data.

In a layer, the time above melt temperature for each pixel is defined as the total time the pixel is above a set threshold. The melt point threshold was determined by observation of the apparent phase transition region in the spatial profile of a melt pool. Figure 3 (a) is the spatial profile of a melt pool showing the apparent phase transition region corresponding to 12,000 counts. Time above melting temperature is proportionate to the apparent melt pool size. This is explained by the time series data from a pixel in Fig. 3 (b). Due to the raster of the laser during processing the apparent melt pool will pass over a pixel several times for a layer. Larger apparent melt pools results in the pixel measuring values above the melt temperature threshold more times than smaller melt pools. In Fig. 3 (b) the pixel measured values above the apparent phase transition region six times. The time above the melt temperature was increased each time the melt pool passed over the pixel. This means larger time above melt temperature values are proportionate to larger melt pools while smaller values of time above melt temperature correspond to smaller melt pools.
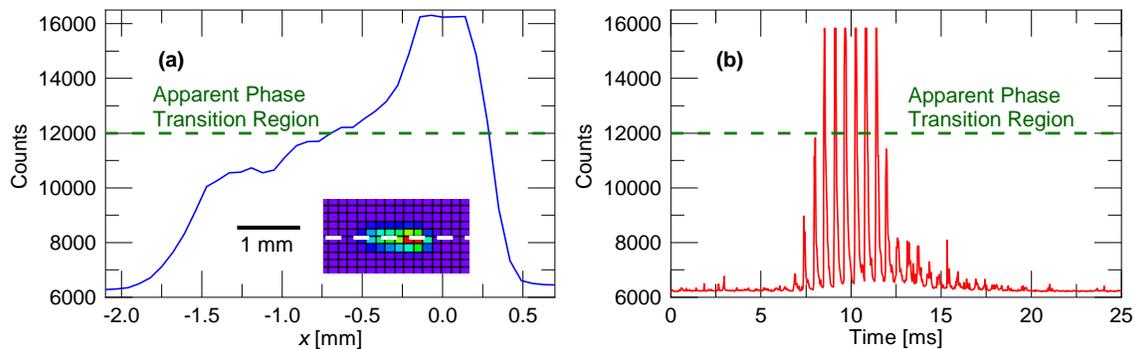
FIG 3: (a) Apparent phase transition region in spatial profile of melt pool and (b) temporal thermal data for single pixel.

The other metrics extracted from the thermal data including maximum gradient and maximum cooling rate are direct calculations. The feature of maximum gradient is determined by calculating the spatial derivative for each frame in the time-series data and extracting the maximum value a pixel experiences. The maximum cooling rate is determined by calculating the temporal derivative and then extracting the maximum reduction of counts from one frame to the next for

each pixel. Figure 4 consists of color maps of time above the melt temperature, maximum gradient, and maximum cooling rate for a single layer in the gage length of the tensile test specimen manufactured with a laser power of 175 W and exposure time of 50 μs.
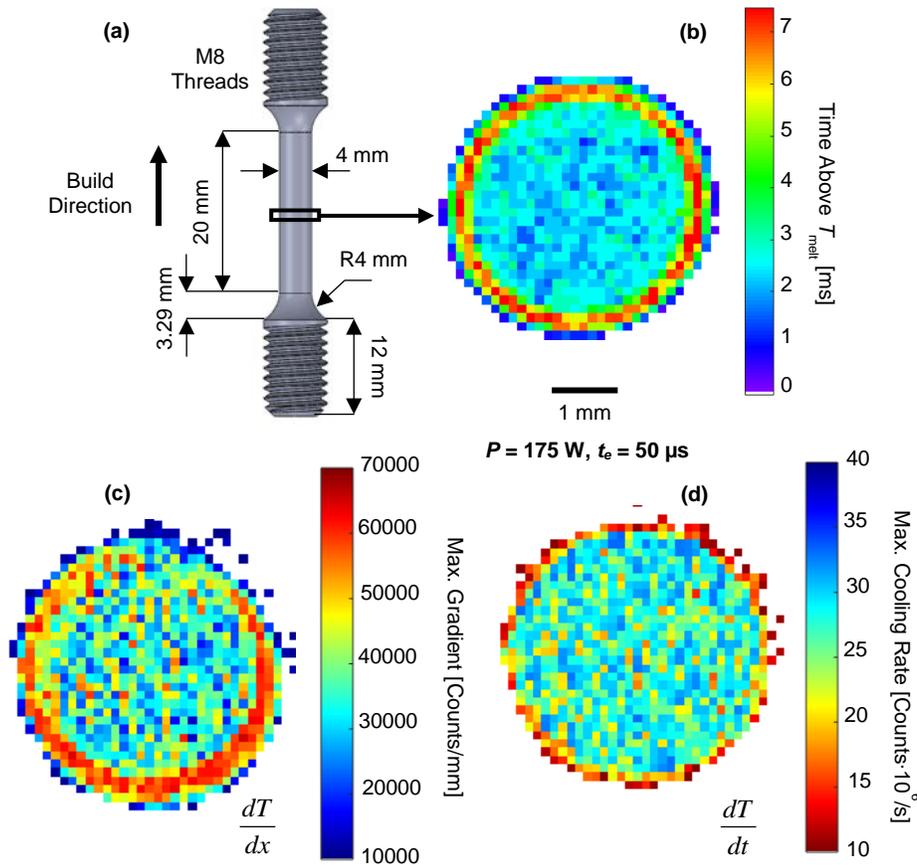
FIG 4: (a) Tensile test specimen geometry and color maps of layer in gage length for thermal features of (b) time above melt temperature, (c) maximum gradient, and (d) maximum cooling rate.

3.2. Voxel Based 3-Dimensional Reconstruction of Parts

The compressed data in Fig. 4 can be generated for each layer of a part. The layer-by-layer data can then be arranged to generate a filtered voxel based 3-Dimensional reconstruction of the part. Figure 5 is an example of a 3-Dimensional reconstruction using time above melt temperature as the voxel filter for one of the tensile test specimen manufactured with a defect introduced into the gage length. The defect introduced into this specimen included specific areas processed with a laser power of 100 W. The rest of the specimen was manufactured using a laser power of 200 W. The voxel based reconstruction can be sliced spatially in any plane. The spatial slice in Fig. 5 is normal to the build plane and clearly shows the defect within the gage length. The 3-Dimensional reconstruction can also be sliced by setting a threshold for the values of the voxel color scale. This is demonstrated in Fig. 5 where a threshold was set to plot voxels with time above the melt temperature values from 0 to 3 ms and then 3 to 6 ms.
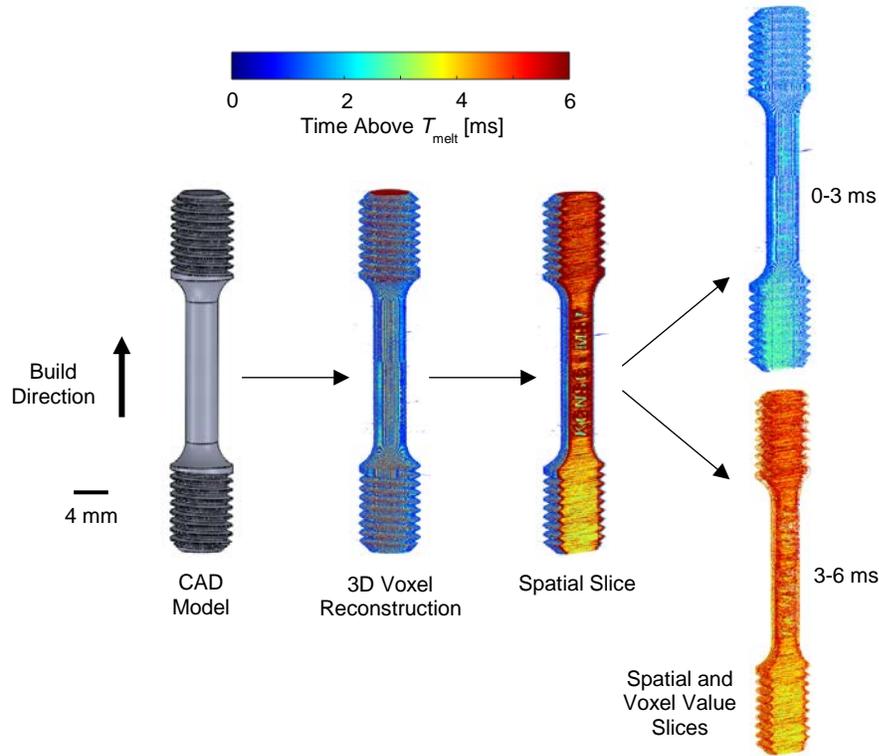
FIG 5: 3D voxel reconstruction of tensile test specimen showing introduced defect in gage length through spatial and color scale slicing.

Figure 6 is further demonstration of defect identification through layer-to-layer process monitoring with SWIR imaging. The reconstructions in Fig. 6 use time above melt temperature as the filter to generate the voxel based representations from the raw thermal data. Figure 6 contains an image of the two tensile specimens manufactured with defects. The defects introduced into these samples were the previously mentioned areas of the gage length processed with lower laser power for the first specimen and then an un-sintered void for the second specimen. It is not possible to differentiate the specimens through optical observations of their exteriors. The interior defects are visible in the voxel data for the tensile test specimens. These defects are highlighted in Fig. 6 through the images of the cross sections of the tensile specimen CAD models and corresponding 3-Dimensional reconstructions. The CAD geometry and voxel data slice for the nominal tensile specimen are also included in Fig. 6. A subtle increase in time above melt temperature can be seen in the voxel reconstruction for the top of the nominal specimen. This is a result of other parts with less layers completing during the build before the nominal tensile test specimen. The layer-to-layer process time was decreased and that led to an increase in the time above melt temperature for the nominal tensile specimens. This change in the thermal history identified through the 3-D voxel reconstruction can potentially be significant and lead to a variation in part properties for extreme cases.
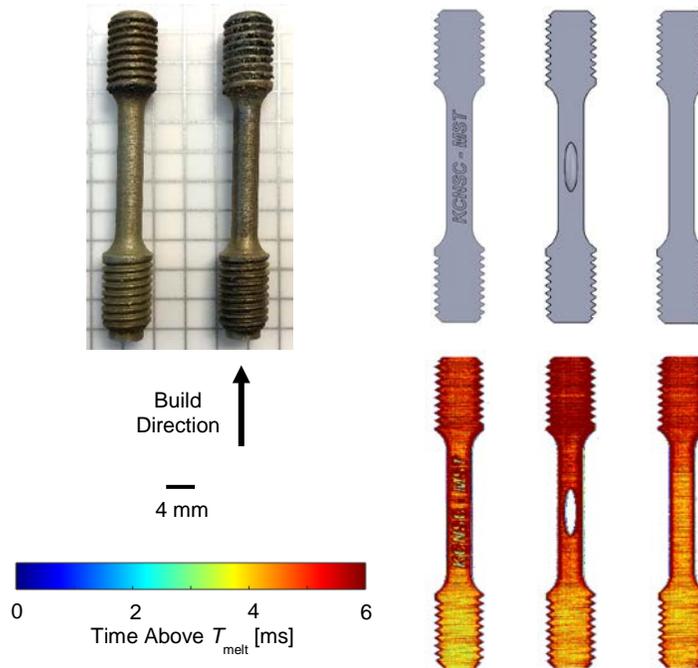
FIG 6: Identification of changes in thermal history and internal defects in tensile test specimens through layer-to-layer process monitoring.

4. Process Parameter and Mechanical Properties Correlations

4.1. Correlation of Thermal Features and Process Parameters

The framework developed to create the filtered voxel data based on thermal features allows layer-to-layer process monitoring and can be used to identify introduced defects in specimens as shown in Fig. 6. This framework can be expanded to evaluate part engineering properties by correlation of the extracted thermal features to experimental data. The three thermal features including time above melt temperature, maximum gradient, and maximum cooling rate will be compared by evaluating the parameter that has the strongest relationship with process parameters and specimen properties.

Figure 7 contains representative time above melt temperature color maps for a layer in the gage length of the tensile test specimens. In Fig. 7, the trend time above melt temperature with respect to process parameters is visible qualitatively, with higher times for larger laser powers and exposure times. The color maps show the borders of the specimens have higher time above melt temperature values. This is due to the laser raster pattern and border scans. At the edges of the part the laser is cornering leading to larger melt pools and after the interior of the part is processed, the border scans trace the perimeter of the part. Both of these features in the process will increase the time above melt temperature.
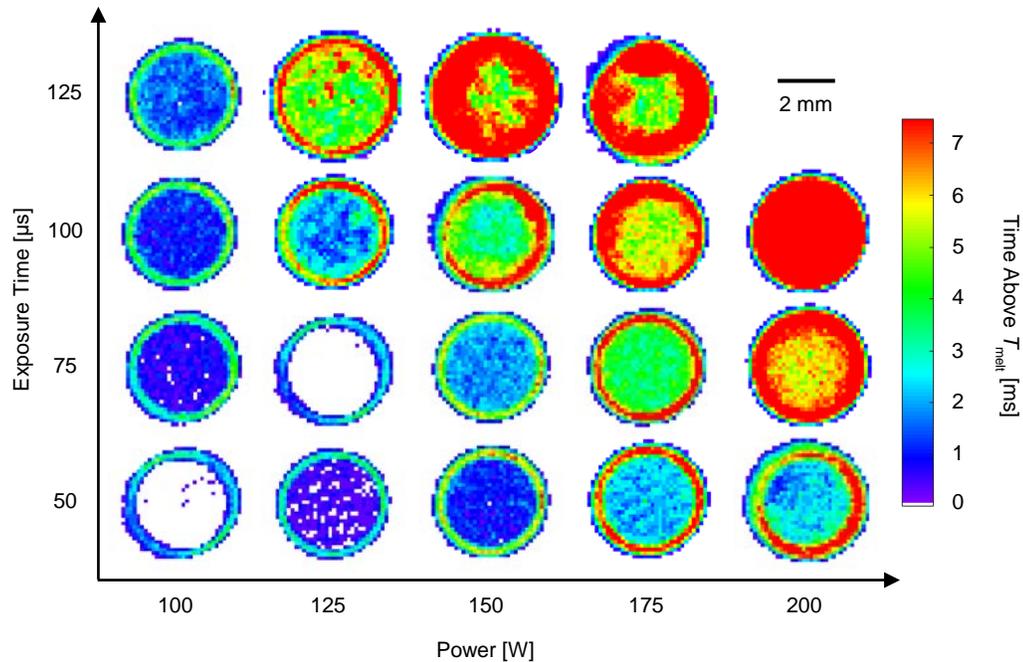
FIG 7: Representative color maps of time above melting temperature for layers in tensile test specimens' gage lengths processed with varied laser power and exposure time.

Data similar to Fig. 7 can be generated for maximum gradient and maximum cooling rate. To evaluate the thermal features as a function of process parameters, time above melt temperature, maximum gradient, and maximum cooling rate were extracted for ten layers of each process parameter combination. The thermal features were averaged for the ten layers excluding data from the edges of the specimens to avoid effects from border scans. The three thermal features are plotted as a function of linear energy density in Fig. 8.

In Fig. 8 (a), the time above melt temperature has a positive correlation with energy density while in Fig. 8 (c) the maximum cooling rate has a negative correlation. The maximum gradient in Fig. 8 (b) appears to have no correlation with energy density. The results for time above melt temperature and maximum cooling rate follow the expected trends. The higher energy densities lead to larger melt pool sizes which is proportionate to increased times above the melt temperature. The increased energy input resulting from the larger energy densities should also lead to the decrease in maximum cooling rate shown in Fig. 8 (c).
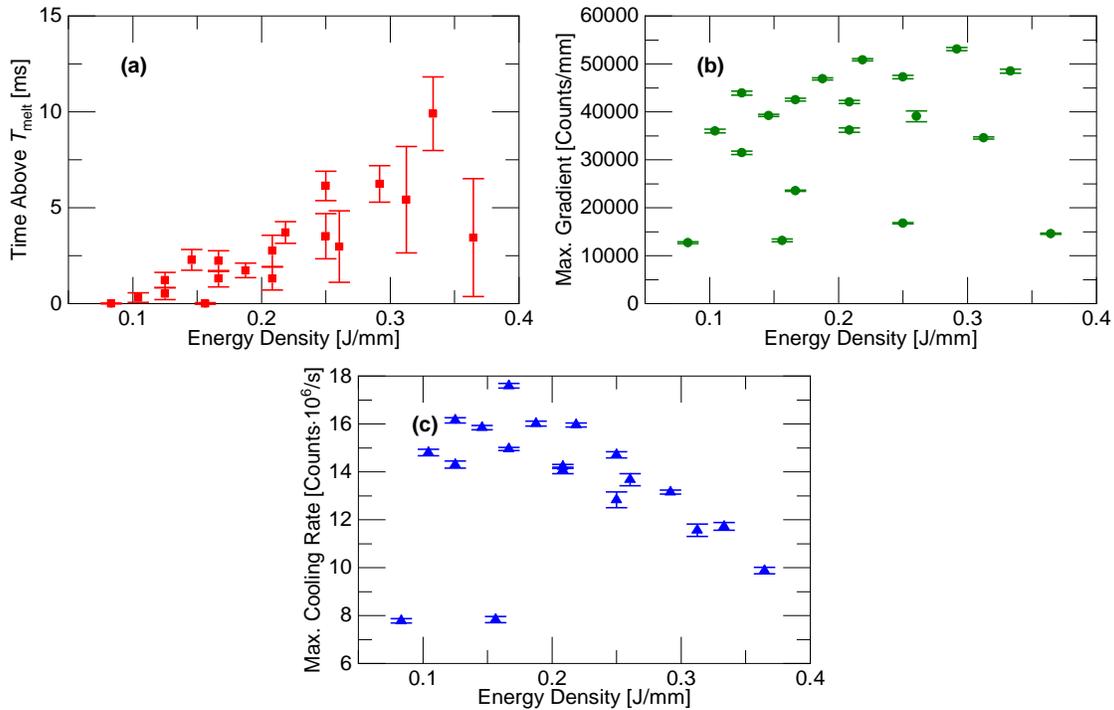
FIG 8: (a) Time above melting temperature, (b) maximum gradient, and (c) maximum cooling rate as a function of linear energy density.

The error bars in Fig. 8 demonstrate the variation of the thermal features from layer-to-layer. The time above the melt temperature experiences higher variance as energy density increases. The maximum gradient and maximum cooling rate have similar variances for all energy densities. The variation within a single layer and from layer-to-layer is possibly due to the laser scan strategy which includes changing scan path partitions and rotation angles for each layer. The increased variance in time above the melt temperature for higher energy densities could be a result of the laser cornering. This effect is illustrated in Fig. 7 by the color map of the specimen processed with a laser power of 175 W and exposure time of 125 µs. The higher energy densities result in larger melt pool sizes leading to larger time above melt temperature values at the edges of the specimens. The center of the specimens experience times above the melt temperature less than the edges. This leads to the larger variance, even with excluding data from the edges of the part that are affected by border scans.

4.2. Correlation of Thermal Features and Mechanical Properties

Both the time above melt temperature and maximum cooling rate were shown to scale with process parameters. Tensile test specimen properties have been correlated to the time above melt temperature, maximum gradient, and maximum cooling rate to further compare the three thermal features. The tensile specimen properties for each process parameter combination were experimentally determined for correlation include yield strength, ultimate strength, microhardness, and porosity.

The tensile tests to determine yield strength and ultimate strength were performed using an Instron 5969 with load control under ASTM E8/E8M standards [6]. Samples were tested in as built

condition after cleaning the threads with a die. In total 95 samples were tested, 5 for each of the 19 successful parameter sets used during manufacturing. Tensile specimen testing was randomly ordered and randomly oriented in the tensile testing machine grips. Vickers microhardness testing was performed with a Struers Duramin 5. The microhardness tests used a force of 490 mN for 13 seconds following ASTM E384-17 standards [7]. Porosity of the tensile test specimen cross-sections was estimated by using image analysis. The tensile test specimens were sectioned in the gage length and polished. Optical micrographs were taken of the cross-sections using a Hirox KH-8700 microscope. ImageJ was then used used to find the percent porosity by converting the image to binary and determining the ratio of the amount of cross-sectional area that was un-sintered to the total area.

Figure 9 is the correlation of specimen properties to time above melt temperature. The peak performance for tensile properties is reached at a time above melt temperature of 2 ms. The microhardness results contain more scatter, but also reach near peak performance at a time above melt temperature of 2 ms. Porosity in samples decreases with increasing time above melt temperature. Four time above melt temperatures above 3 ms resulted in less than 1% porosity. The time above melt temperatures above 3 ms with porosity greater than 2% correspond to the specimens processed with the higher exposure times. The increased porosity for these samples could possibly be due to an increase in keyhole processing at the edges of the parts.
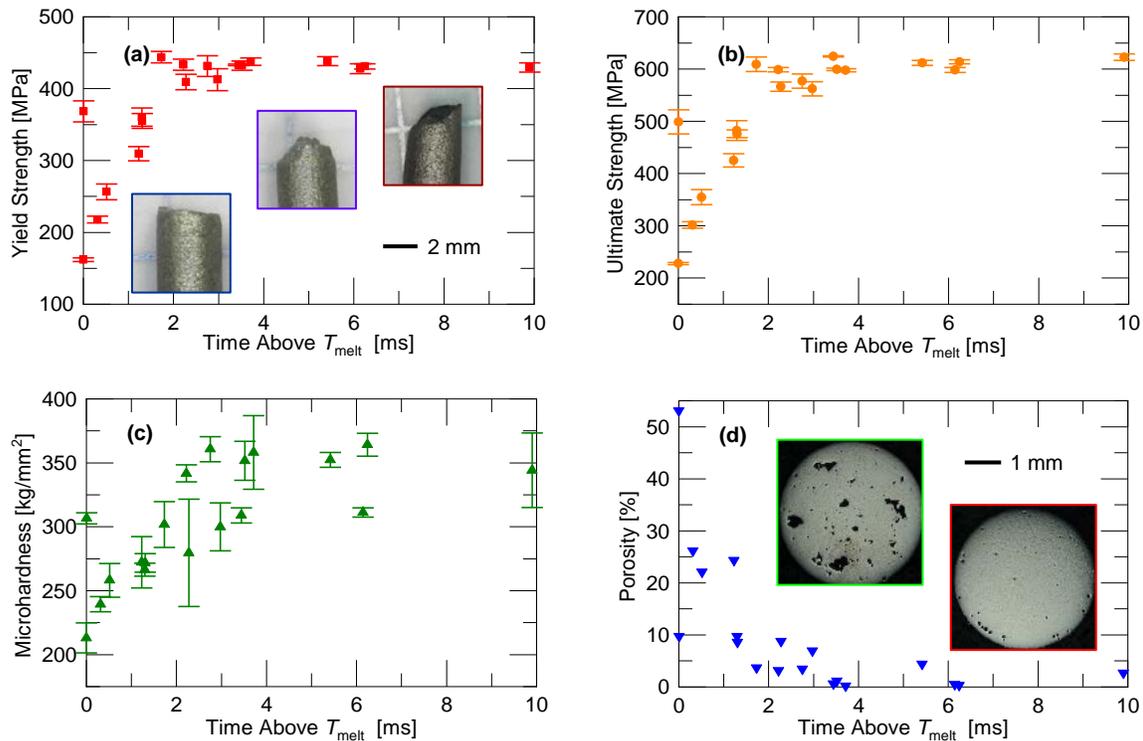
FIG 9: Specimen properties as a function of time above melting temperature.

Figure 10 contains the correlations of specimen properties to the maximum gradient. There are no clear trends for any of the specimen properties as a function of maximum gradient. Figure 11 is the correlation of specimen properties and maximum cooling rate. While maximum cooling

rate correlated to process parameters, there is no clear relationship with specimen properties. The lack of a correlation of maximum gradient and cooling rate to part properties could possibly be explained by uncertainties in the spatial and temporal resolution of the thermal camera data. These uncertainties could lead to issues with the direct calculations of the maximum gradient and maximum cooling rate. The feature of time above melt temperature is not significantly affected by the uncertainties in resolution.
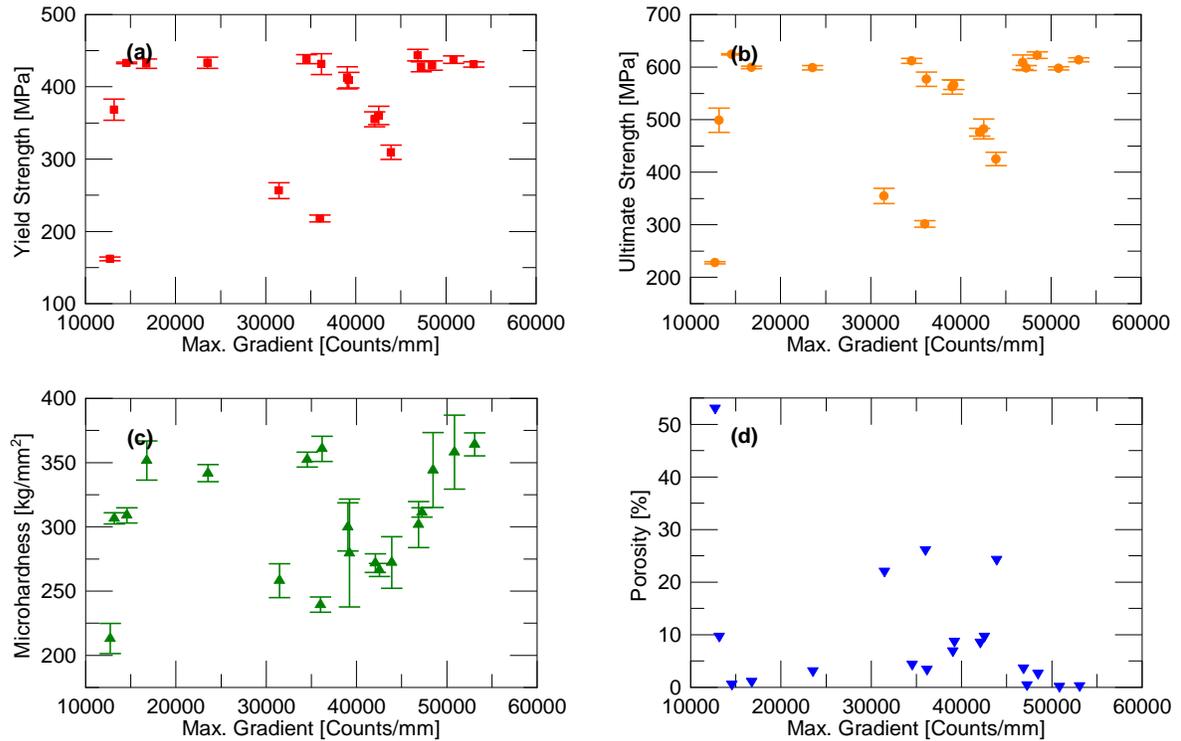
FIG 10: Specimen properties as a function of maximum gradient.
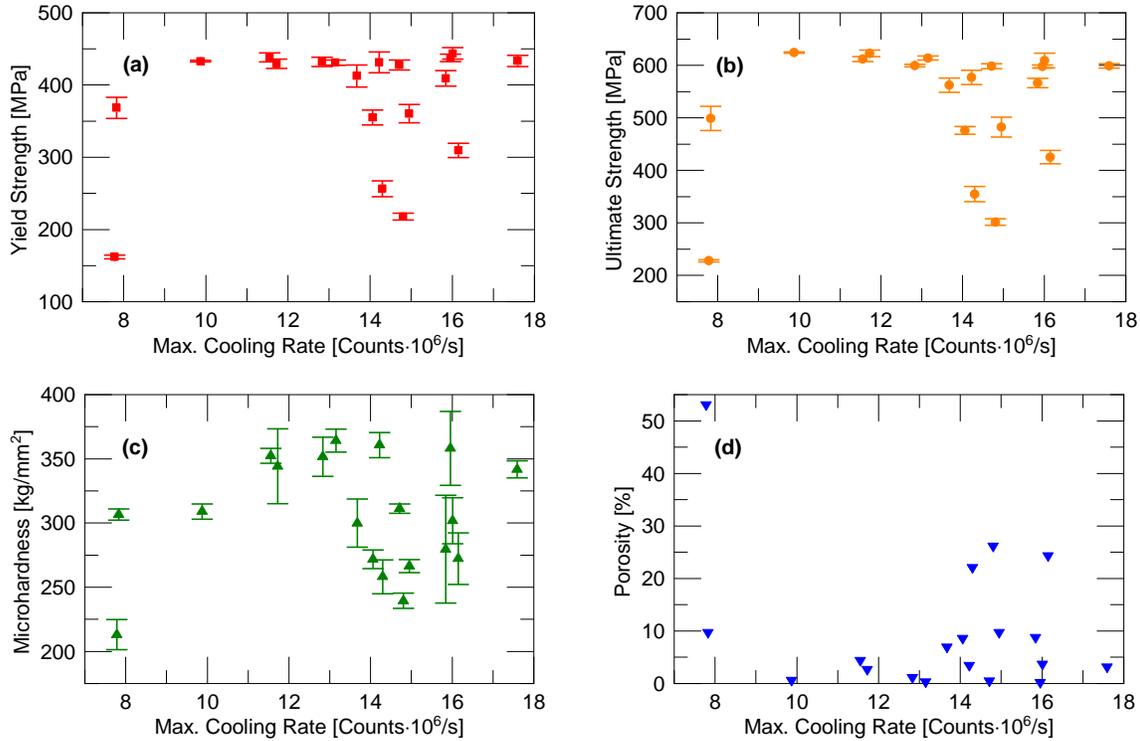
FIG 11: Specimen properties as a function of maximum cooling rate.

5. Summary and Conclusions

In this paper, a framework was developed to compress time series SWIR imaging data collected during layer-to-layer process monitoring into filtered voxel based 3-Dimensional reconstructions of SLM manufactured tensile specimens. The filter for the voxel data was determined by the feature extracted from the thermal data. The features in this paper extracted were time above melt temperature, maximum gradient, and maximum cooling rate. The framework was then used with time above melt temperature as the filter for preliminary identification of introduced defects in the gage length of tensile specimens through the monitoring of layer-to-layer part quality. The 3-Dimensional reconstructions of the specimens can be sliced spatially in any plane for analysis. In addition to spatial slicing, thresholds can be set to slice the data based on the thermal feature.

After demonstration of layer-to-layer process monitoring the three thermal features were compared by evaluating their correlations to process parameters and specimen properties. Both time above the melt temperature and maximum cooling late were shown to correlate with the linear energy density used during manufacturing of the tensile test specimens with varied laser power and exposure time. Maximum gradient did not correlate with linear energy density. The time above melt temperature also correlated well with the part properties of yield strength, ultimate strength, microhardness, and porosity. A value of time above melt greater than 2 ms resulted in peak performance for the mechanical properties. The specimen porosity was generally a minimum for times above melt temperature greater than 3 ms. The maximum gradient and maximum cooling rate had no clear correlations with the specimen properties.

The time above melt temperature had the strongest relationship to part properties out of the three thermal features compared in this paper. The direct calculations of maximum gradient and maximum cooling rate possibly did not correlate well due to uncertainties in the spatial and temporal resolution of the SWIR imaging camera. The correlation of the thermal feature of time above melt temperature to part properties shows meaningful data can be extracted from SWIR imaging data for potential use in layer-to-layer control of the SLM process. This thermal feature is easily computed and can be implemented in a controls oriented decision making process. Ensuring a uniform time above melt across a layer through controls could result in an increase in mechanical property homogeneity.

The framework developed for layer-to-layer process monitoring can be expanded to incorporate more thermal features extracted from the time series data captured for a layer during SLM. Features with strong correlations to part properties such as time above melt temperature can be used in further development of the framework. The correlations between the thermal features and part properties could potentially be used to generate voxel based data of localized mechanical properties. This development in future work will allow layer-to-layer part monitoring to ensure part quality and flag defects during the SLM manufacturing process based on engineering properties.

6. Acknowledgement

7. References

[1] Krauss H, Eschey C, Zaeh M. Thermography for monitoring the selective laser melting process. Solid Freeform Fabrication Symposium. 2012.

[2] Grasso M, Demir A, Previtali B, Colosimo B. In situ monitoring of selective laser melting of zinc powder via infrared imaging of the process plume. Robotics and Computer-Integrated Manufacturing. 2018; 49:229-39.

[3] Yadroitsev I, Krakhmalev P, Yadroitsava I. Selective laser melting of Ti6Al4V alloy for biomedical applications: Temperature monitoring and microstructural evolution. Journal of Alloys and Compounds. 2014; 583:404-9.

[4] Heigel J, Lane B. The effect of powder on cooling rate and melt pool length measurements using in situ thermographic techniques. Solid Freeform Fabrication Symposium. 2017.

[5] Cheng B, Lydon J, Cooper K, Cole V, Northrop P, Chou K. Infrared thermal imaging for melt pool analysis in SLM: a feasibility investigation. Virtual and Physical Prototyping. 2018; 13:8-13.

[6] ASTM E8/E8M Standard Test Methods for Tension Testing of Metallic Materials, ASTM International, West Conshohocken, PA, 2016.

[7] ASTM E384-17 Standard Test Method for Microindentation Hardness of Materials, ASTM International, West Conshohocken, PA, 2018.